Unexpected Spin-Crossover and a Low-Pressure Phase Change in an Iron(II)/Dipyrazolylpyridine Complex Exhibiting a High-Spin Jahn–Teller Distortion

Laurence J. Kershaw Cook,[†] Flora L. Thorp-Greenwood,[†] Tim P. Comyn,[‡] Oscar Cespedes,[§] Guillaume Chastanet,*,[∥] and Malcolm A. Halcrow*,[†]

[†]School of Chemistry, University of Leeds, Woodhouse Lane, Leeds LS2 9JT, United Kingdom

[‡]Institute for Materials Research, School of Chemical and Process Engineering, University of Leeds, Leeds LS2 9JT, United Kingdom

[§]School of Physics and Astronomy, University of Leeds, E. C. Stoner Building, Leeds LS2 9JT, United Kingdom

[∥]CNRS, Université de Bordeaux, ICMCB, UPR 9048, F-33600 Pessac, France

S *Supporting Information*

ABSTRACT: The synthesis of 4-methyl-2,6-di(pyrazol-1-yl)-pyridine (L) and four salts of $[FeL_2]X_2$ ($X^- = BF_4^-$, **1**; $X^- = ClO_4^-$, **2**; $X^- = PF_6^-$, **3**; $X^- = CF_3SO_3^-$, **4**) are reported. Powder samples of **1** and **2** both exhibit abrupt, hysteretic spin-state transitions on cooling, with $T_{1/2}\downarrow = 204$ and $T_{1/2}\uparrow = 209$ K (**1**), and $T_{1/2}\downarrow = 175$ and $T_{1/2}\uparrow = 193$ K (**2**). The 18 K thermal hysteresis loop for **2** is unusually wide for a complex of this type. Single crystal structures of **2** show it to exhibit a Jahn–Teller-distorted six-coordinate geometry in its high-spin state, which would normally inhibit spin-crossover. Bulk samples of **1** and **2** are isostructural by X-ray powder diffraction, and undergo a crystallographic phase change during their spin-transitions. At temperatures below $T_{1/2}$, exposing both compounds to 10^{-5} Torr pressure inside the powder diffractometer causes a reversible transformation back to the high-temperature crystal phase. Consideration of thermodynamic data implies this cannot be accompanied by a low → high spin-state change, however. Both compounds also exhibit the LIESST effect, with **2** exhibiting an unusually high T(LIESST) of 112 K. The salts **3** and **4** are respectively high-spin and low-spin between 3 and 300 K, with crystalline **3** exhibiting a more pronounced version of the same Jahn–Teller distortion.
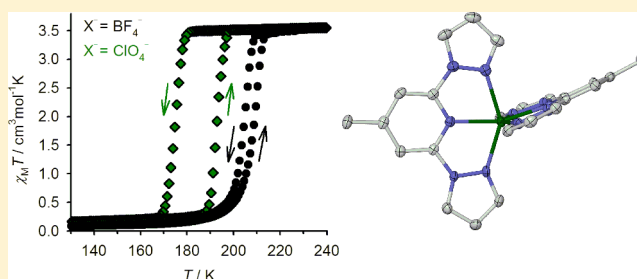
INTRODUCTION

The $[Fe(1\text{-bpp})_2]^{2+}$ series of complexes, where 1-bpp is a derivative of 2,6-di(pyrazol-1-yl)pyridine,[1−3] is one of the most widely studied systems in spin-crossover research.[4−8] Their popularity has arisen because they often undergo spin-crossover near room temperature, and due to the flexibility of the bpp ligand synthesis which allows every position of the ligand framework to be derivatized.[1,3] However, a complicating factor in their chemistry is that high-spin $[Fe(1\text{-bpp})_2]^{2+}$ derivatives are prone to exhibiting a type of angular Jahn–Teller distortion (Chart 1).[9] This is manifested by a reduction of the *trans*-N{pyridyl}−Fe−N{pyridyl} angle (ϕ) below its ideal value of 180°, and/or a twisting of the two tridentate ligands from the perpendicular ($\theta < 90°$, where θ is the dihedral angle between the least-squares planes of the ligands).[9−17] The two components of the distortion can occur independently in the same compound, and take the values $155 \leq \phi \leq 180°$ and $60 \leq \theta \leq 90°$.[1] The most extreme examples of the distortion are often associated with close secondary contacts in the crystal between the complex and neighboring anions or lattice solvent.[3] There are examples of the same high-spin compound crystallizing in distorted and undistorted polymorphs;[13] of

Chart 1. Components of the Jahn−Teller Distortion in High-Spin $[Fe(1\text{-bpp})_2]^{2+}$ Complexes[a] ($X^- = BF_4^-$, ClO_4^-, etc,)[9]
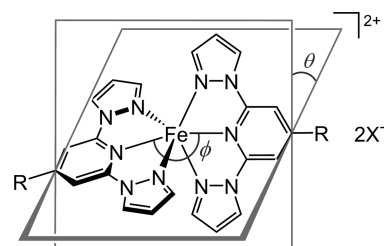
[a]Undistorted complexes have $\phi = 180°$ and $\theta = 90°$. $[Fe(1\text{-bpp})_2]^{2+}$ itself has R = H, while $[FeL_2]^{2+}$ has R = Me.

different salts of the same complex adopting distorted and undistorted structures,[9] and of distorted and undistorted molecules cocrystallizing in the same material.[11,14] In principle, this type of Jahn−Teller distortion can occur in any complex of

Table 1. Experimental Details for the Crystal Structure Determinations of the Complexes in This Study

	1·4MeNO$_2$	**2·4MeNO$_2$**	**2**		**3**
formula	C$_{28}$H$_{34}$B$_2$F$_8$FeN$_{14}$O$_8$	C$_{28}$H$_{34}$Cl$_2$FeN$_{14}$O$_{16}$	C$_{24}$H$_{22}$Cl$_2$FeN$_{10}$O$_8$	C$_{24}$H$_{22}$Cl$_2$FeN$_{10}$O$_8$	C$_{24}$H$_{22}$F$_{12}$FeN$_{10}$P$_2$
fw	924.16	949.44	705.27	705.27	796.31
cryst syst	tetragonal	tetragonal	monoclinic	monoclinic	monoclinic
space group	$I\bar{4}c2$	$I\bar{4}c2$	$P2_1/n$	$P2_1/n$	$C2/c$
a/Å	16.2226(3)	16.3995(3)	8.4719(3)	8.5607(8)	22.1424(11)
b/Å			8.5349(3)	8.6545(6)	10.9900(4)
c/Å	14.8493(5)	14.9340(7)	39.1597(12)	39.632(3)	15.2542(6)
β/deg			91.010(3)	90.812(8)	123.231(3)
V/Å^3	3907.93(17)	4016.4(2)	2831.07(17)	2936.0(4)	3105.0(2)
Z	4	4	4	4	4
T/K	100(2)	150(2)	100(2)	240(2)	100(2)
D_{calcd}/g cm^{-3}	1.571	1.570	1.655	1.596	1.703
reflns collected	10 584	28 479	8717	9230	11 544
unique reflns	2478	4861	4951	5406	3812
R_{int}	0.054	0.020	0.026	0.062	0.042
R1, $I > 2\sigma(I)^a$	0.081	0.059	0.033	0.098	0.038
wR2, all data^b	0.195	0.141	0.086	0.249	0.087
GOF	1.157	1.184	1.037	1.096	1.057

^{a}R $= \sum[|F_o| - |F_c|]/\sum|F_o|$. ^{b}wR $= [\sum w(F_o{}^2 - F_c{}^2)/\sum wF_o{}^4]^{1/2}$.

Table 2. Selected Bond Lengths (Å) and Angular Parameters (deg) in the Crystal Structures of the Complexes in This Work^a

	1·4MeNO$_2$^{b}	**2·4MeNO$_2$^{b}**	**2**	**2**	**3^c**
T/K	100	150	240	100	100
Fe−N{pyridyl}	1.894(5)	1.894(2)	2.126(6), 2.137(6)	2.1236(19), 2.1354(19)	2.1479(15)
Fe−N{pyrazolyl}	1.981(5)	1.971(2)	2.159(6)−2.241(7)	2.1642(18)−2.2417(19)	2.1774(16), 2.1877(16)
α	79.78(13)	80.05(6)	73.5(4)	73.30(14)	72.73(8)
Σ	89.2(7)	86.4(3)	150.2(9)	156.1(2)	173.6(2)
Θ	292	283	470	478	517
ϕ	180	180	163.7(2)	160.06(7)	157.92(9)
θ	90	90	89.48(7)	89.62(2)	67.70(2)

$^a\alpha$, Σ, and Θ are indices showing the spin state of the complex,[38,39] while θ and ϕ are measures of the angular Jahn−Teller distortion sometimes shown by these iron centers in their high-spin state (Chart 1).[1,9−14] Typical values for all these parameters in high- and low-spin [Fe(1-bpp)$_2$]$^{2+}$ derivatives are given in ref 1. ^{b}The asymmetric unit of this compound contains one-quarter of a complex molecule, with crystallographic $\bar{4}$ symmetry. ^{c}The asymmetric unit of this compound contains half a complex molecule, with crystallographic C_2 symmetry.

high-spin d^5 and d^6 metal ions with meridional tridentate ligands. Strongly distorted examples are relatively rare in practice, however,[18−20] and the distortion is more prevalent in [Fe(1-bpp)$_2$]$^{2+}$ chemistry than in any other series of compounds. That may reflect the narrow ligand chelate bite angle in high-spin [Fe(1-bpp)$_2$]$^{2+}$ centers (ca. 73°).[9]

Since the distortion only occurs in the high-spin form, spin-crossover in solid [Fe(1-bpp)$_2$]$^{2+}$ derivatives is inhibited if their molecular distortion is too pronounced. In that case, the large structural rearrangement required to convert the distorted high-spin state into an undistorted low-spin state is prohibited by the rigidity of the surrounding solid lattice.[17] This has led to several [Fe(1-bpp)$_2$]$^{2+}$ derivatives that should exhibit spin-crossover, all other things being equal, being inactive to spin-crossover in the solid state. A survey of these compounds six years ago concluded that solid complexes with $\phi < 172°$ and/or $\theta < 76°$ should remain trapped in their high-spin form on cooling.[1] However, we now report a new example [FeL$_2$][ClO$_4$]$_2$ (L = 4-methyl-2,6-di(pyrazol-1-yl)pyridine), which exhibits a much more pronounced distortion when freshly crystallized and yet exhibits a cooperative spin transition with a significant thermal hysteresis.

■ EXPERIMENTAL SECTION

All reagents were purchased commercially and used as supplied unless otherwise stated, although diglyme was dried over sodium before use.

Synthesis of 4-Methyl-2,6-di(pyrazol-1-yl)pyridine (L). Pyrazole (1.26 g, 18.5 mmol) was dissolved in diglyme (20 cm^3) under a N$_2$ atmosphere. Sodium hydride (60% suspension in mineral oil; 0.74 g, 18.5 mmol) was added, and the mixture was left to stir for 30 min. 4-Methyl-2,6-dichloropyridine (1.0 g, 6.2 mmol) was then added in one portion, and the reaction was heated at 130 °C for 3 days. The reaction mixture was cooled and quenched with excess water. The resultant white precipitate was filtered, washed with diethyl ether, and dried *in vacuo*. Yield 0.98 g, 70%. Mp 88−90 °C. Elemental analysis for C$_{12}$H$_{11}$N$_5$ found (calcd) (%) C 64.4 (64.0), H 5.20 (4.92), N 30.9 (31.1). HR ESMS m/z 226.1085 (calcd for [Hbpp^{Me}]$^+$ 226.1087). ^{1}H NMR (CDCl$_3$) δ 2.48 (s, 3H, CH_3), 6.48 (dd, 1.7 and 2.6 Hz, 2H, Pz H^4), 7.69 (s, 2H, Py $H^{3/5}$), 7.75 (d, 1.7 Hz, 2H, Pz H^3), 8.55 (d, 2.6 Hz, 2H, Pz H^5). ^{13}C NMR (CDCl$_3$) δ 21.6 (1C, CH_3), 107.8 (2C, Pz C^4), 110.1 (2C, Py $C^{3/5}$), 127.1 (2C, Pz C^5), 142.2 (2C, Pz C^3), 150.0 (1C, Py C^4), 153.5 (2C, Py $C^{2/6}$).

Synthesis of Complexes. The same basic method, described below for [FeL$_2$][BF$_4$]$_2$, was used for all the complexes in this work. A solution of L (0.20 g, 0.88 mmol) and Fe[BF$_4$]$_2$·6H$_2$O (0.15 g, 0.44 mmol) in nitromethane (15 cm^3) was refluxed until all the solid had dissolved (ca. 2 h). The cooled solution was concentrated *in vacuo* to ca. 5 cm^3. Slow diffusion of diethyl ether vapor into the filtered solution afforded yellow crystals of the product. The other complex salts were prepared by analogous reactions using the appropriate iron

precursor $Fe[ClO_4]_2 \cdot 6H_2O$, $Fe[CF_3SO_3]_2$, or $Fe[PF_6]_2$ (prepared *in situ* by stirring $FeCl_2 \cdot 4H_2O$ with 2 equiv of NH_4PF_6). Recrystallized yields ranged from 34% to 87%. Elemental analysis data for the compounds are listed below.

  [FeL₂][BF₄]₂ (1). $C_{24}H_{22}B_2F_8FeN_{10}$ found (calcd) (%) C 42.6 (42.4), H 3.50 (3.26), N 20.3 (20.6).

  [FeL₂][ClO₄]₂ (2). $C_{24}H_{22}Cl_2FeN_{10}O_8$ found (calcd) (%) C 40.8 (40.9), H 3.10 (3.14), N 19.9 (19.9).

  [FeL₂][PF₆]₂ (3). $C_{24}H_{22}F_{12}FeN_{10}P_2$ found (calcd) (%) C 36.4 (36.2), H 2.70 (2.78), N 17.3 (17.6).

  [FeL₂][CF₃SO₃]₂·¹/₂H₂O (4·¹/₂H₂O). $C_{26}H_{22}F_6FeN_{10}O_6S_2 \cdot {}^1/_2H_2O$ found (calcd) (%) C, 38.1 (38.4), H 2.65 (2.85), N 17.0 (17.2).

  *Caution! Although we have experienced no problems in handling compound **2**, metal−organic perchlorates are potentially explosive and should be handled with due care in small quantities.*

Single Crystal X-ray Structure Determinations. Diffraction data for **2**·4MeNO₂ were measured using a Bruker X8 Apex diffractometer, with graphite-monochromated Mo Kα radiation ($\lambda = 0.710\,73$ Å) generated by a rotating anode. All the other diffraction data were collected with an Agilent Supernova dual-source diffractometer using monochromated Mo Kα ($\lambda = 0.710\,73$ Å) or Cu Kα radiation ($\lambda = 1.541\,84$ Å). Both diffractometers were fitted with Oxford Cryostream low-temperature devices. Experimental details of the structure determinations are given in Table 1. All the structures were solved by direct methods (*SHELXS97*[21]), and developed by full least-squares refinement on F^2 (*SHELXL97*[21]). Crystallographic figures were prepared using *XSEED*.[22] Unless otherwise stated, all non-H atoms in the structures were refined anisotropically, and C-bound H atoms were placed in calculated positions and refined using a riding model.

The crystals of **1**·4MeNO₂ and **2**·4MeNO₂ are isostructural. Their asymmetric units contain one-quarter of a formula unit, with Fe(1) lying on the $\overline{4}$ site 1, $^1/_2$, 1 and N(2), C(5), and C(11) on the C_2 axis, x, $^3/_2 - x$, 0; a complete half an ion close to the C_2 axis x, x, $^3/_4$; and a disordered nitromethane molecule lying on a general position. The half an ion in **1** was modeled with refined B−F and F···F distance restraints, but the anion in the ClO_4^- salt refined satisfactorily without restraints. The nitromethane molecule was modeled with fixed distance restraints over two orientations, whose occupancies refined to 0.60 and 0.40 in both structures. All non-H atoms except the minor solvent disorder site were refined anisotropically.

Two data sets were recorded from the same crystal of solvent-free **2**, at 240 K (when the compound is expected to be high-spin), and at 100 K following rapid cooling of the crystal. Cooling the crystals more slowly led them to darken in color and crack around 160 K. No disorder is present in the 100 K structure, which was refined without restraints. The 240 K structure is of lower quality, reflecting extensive disorder in both ClO_4^- anions. These were both modeled over three sites, using refined distance restraints. All the wholly occupied non-H atoms, plus the partial Cl atoms, were refined anisotropically at this temperature.

The asymmetric unit of **3** contains half a formula unit with Fe(1) spanning the crystallographic C_2 axis at 0, y, $^1/_4$. No disorder was detected during this refinement, and no restraints were applied.

Other Measurements. Elemental microanalyses were performed by the University of Leeds School of Chemistry microanalytical service. Electrospray mass spectra (ESMS) were obtained on a Bruker MicroTOF spectrometer, from MeCN feed solutions. All mass peaks have the correct isotopic distributions for the proposed assignments. NMR spectra were obtained using a Bruker Avance 500 FT spectrometer, operating at 500.1 MHz (^{1}H) or 125 MHz (^{13}C). The differential scanning calorimetry measurement used a TA Instruments DSC Q20 calorimeter, heating at a rate of 5 K min⁻¹. X-ray powder diffraction data were obtained with a Bruker D8 Advance A25 diffractometer, using Cu Kα radiation ($\lambda = 1.5418$ Å). Magnetic susceptibility measurements were performed on a Quantum Design VSM SQUID magnetometer, in an applied field of 5000 G and a temperature ramp of 2 K min⁻¹. Diamagnetic corrections for the samples were estimated from Pascal's constants;[23] a previously

measured diamagnetic correction for the sample holder was also applied to the data.

Photomagnetic measurements were performed using a set of photodiodes coupled via an optical fiber to the cavity of a MPMS-55 Quantum Design SQUID magnetometer operating at 2000 G. The powder sample was prepared in a thin layer (~0.1 mg) to promote full penetration of the irradiated light. The sample mass was obtained by comparison with the thermal spin transition curve measured on a larger, accurately weighed polycrystalline sample. The sample was first slow cooled to 10 K, ensuring that potential trapping of HS species at low temperatures did not occur. Irradiation was carried out at a set wavelength, and the power of the sample surface was adjusted to 5 mW cm⁻². Once photosaturation was reached, irradiation was ceased. The temperature was increased at a rate of 0.3 K min⁻¹ to ~100 K and the magnetization measured every 1 K to determine the T(LIESST) value (LIESST = light induced excited spin-state trapping) given by the minimum of the $\delta\chi_M T/\delta T$ versus T curve for the relaxation.[24−26] The T(LIESST) value describes the limiting temperature above which the light-induced magnetic high-spin information is erased in a SQUID cavity. In the absence of irradiation, the magnetization was also measured over the temperature range 10−290 K to follow the thermal spin transition and to obtain a low temperature baseline. Kinetic studies of LIESST relaxation were performed by irradiating the sample at 10 K until photosaturation, and then, under constant irradiation the sample was warmed to a desired temperature around the T(LIESST) region. At the desired temperature, irradiation is stopped, and the decay of the magnetization signal was followed for several hours, or until complete relaxation back to the low-spin baseline.

■ RESULTS AND DISCUSSION

Synthesis and Spin-State Properties of the Complexes. The new ligand L was synthesized via the usual synthetic procedure for 1-bpp derivatives, by the treatment of 2,6-dichloro-4-methylpyridine with 2.5 equiv of sodium pyrazolide in hot diglyme.[27] The four complex salts $[FeL_2]X_2$ ($X^- = BF_4^-$, **1**; $X^- = ClO_4^-$, **2**; $X^- = PF_6^-$, **3**; $X^- = CF_3SO_3^-$, **4**) were obtained by treatment of L with 0.5 equiv of the appropriate iron(II) salt, and recrystallized from $MeNO_2/Et_2O$ solvent mixtures. The bulk materials are all solvent free by microanalysis except for the triflate salt, whose analysis is better reproduced by a hemihydrate formulation.

Rapidly precipitated **1** and **2** are high-spin at room temperature and undergo abrupt, hysteretic spin-transitions on cooling. The transition temperatures by SQUID magnetometry are $T_{1/2}\downarrow = 204$ and $T_{1/2}\uparrow = 209$ K for **1**, and $T_{1/2}\downarrow = 175$ and $T_{1/2}\uparrow = 193$ K for **2**, giving hysteresis widths of 5 and 18 K, respectively (Figure 1). Abrupt spin-transitions with 1−4 K
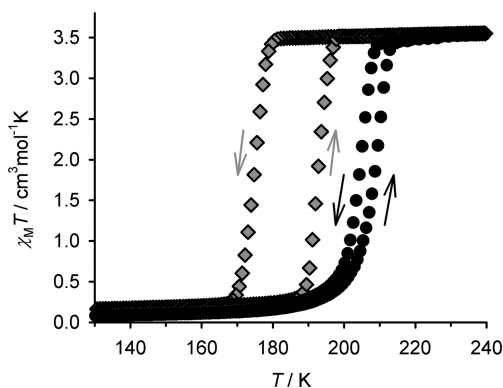
Figure 1. Variable temperature magnetic susceptibility data for **1** (●) and **2** (◆), measured with cooling and warming temperature ramps at a scan rate of 2 K min⁻¹.

hysteresis are quite common in salts of $[Fe(1\text{-}bpp)_2]^{2+}$ derivatives,[9,14,28−31] and are often associated with a particular form of crystal packing (the "terpyridine embrace").[32] Examples with wider hysteresis are rarer,[15,33−35] and excepting two compounds exhibiting stepped spin-transitions with multiple crystallographic phase changes,[34,35] the 18 K hysteresis in **2** is the widest yet reported for a $[Fe(1\text{-}bpp)_2]^{2+}$ complex salt. The spin-transition in **1** was confirmed by a DSC measurement, which showed $T_{1/2}\downarrow$ = 205.2, $T_{1/2}\uparrow$ = 213.0 K, ΔH = 10.8(2) kJ mol^{-1}, and ΔS = 52(1) J mol^{-1} K^{-1}. These thermodynamic parameters are typical for spin-transitions in solid iron(II) complexes.[36] A DSC measurement for **2** was featureless, because its spin-transition in cooling mode lies outside the temperature range of our calorimeter ($T \geq$ 185 K). Bulk samples of **3** are high-spin between 3 and 300 K, while $4\cdot{}^{1}/_{2}H_2O$ is predominantly low-spin over the same temperature range (Supporting Information).

Single Crystal X-ray Diffraction. Slow diffusion of Et$_2$O vapor into MeNO$_2$ solutions of **1** and **2** yields mixtures of brown and yellow crystals with similar block-like morphologies. The brown crystals predominate in both compounds, and were proven to be isostructural solvate phases of formula $1\cdot4MeNO_2$ and $2\cdot4MeNO_2$. The complex molecules in these phases have crystallographically imposed $\bar{4}$ symmetry, and are low-spin according to their metric parameters at the temperature of measurement, 100 or 150 K (Figure 2, Table 1). While higher temperature analyses of these solvates were not undertaken, their brown coloration at 298 K, which is unchanged upon cooling, implies they are also low-spin at room temperature. The anions and solvent occupy square channels in the lattice of approximately 6 × 6 Å^2 running parallel to the c axis, while neighboring complex dications only interact through van der Waals contacts (Supporting Information).

Structural analysis of the solvent-free yellow crystals was only achieved for **2**. Cooling the crystals slowly (ca. 2 K min^{-1}) on the diffractometer caused them to darken in color and crack near 160 K, which is close to the spin-transition temperature in the bulk material. A data collection from a cracked crystal at 100 K showed it to be badly twinned, and its structure could not be solved. However, the crystals sometimes retained their integrity, and their yellow color, upon more rapid cooling to 100 K at ca. 6 K min^{-1}. This reflects kinetic trapping of the material in its high-spin state, which is metastable below 160 K. At these low temperatures the lattice has insufficient thermal energy to relax to its low-spin ground state. Such thermally induced excited-spin-state trapping (TIESST) behavior is well-known for materials whose thermal spin-crossover occurs below 200 K, as in **2**.[37] Attempts to access the low-spin state of **2** by rapidly quenching a crystal to 100 K, then slowly rewarming, led to decomposition of the crystal above 120 K which is close to its high-spin → low-spin thermal relaxation temperature (see below).

Structure refinements of **2** were performed at 240 K and at 100 K, in its thermodynamic and kinetically trapped high-spin states (Figure 2). The refinement is better quality at 100 K than at 240 K, owing to the presence of anion disorder at the higher temperature. The most noteworthy aspect of these structures is that **2** exhibits a typical Jahn−Teller distortion for this type of compound. The distortion only occurs in ϕ, which is 160.06(7)° at 100 K; θ is essentially equal to its ideal value of 90° (Chart 1). The distortion is slightly smaller at 240 K than at 100 K, through an increase in ϕ to 163.7(2)°. That is also reflected in the inner coordination sphere of the complex,
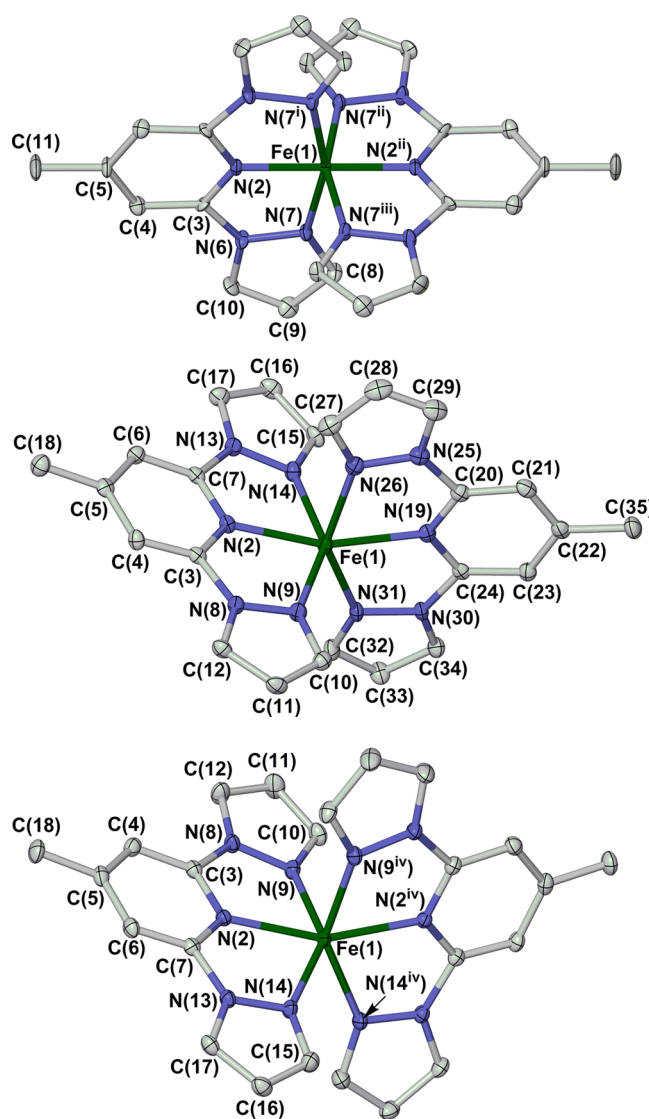
Figure 2. Views of the $[FeL_2]^{2+}$ dications in the crystal structures of $1\cdot4MeNO_2$ (top), **2** at 100 K (center), and **3** (bottom). Displacement ellipsoids are at the 50% probability level. Symmetry codes: (i) $^3/_2 - y$, $^3/_2 - x$, $2 - z$; (ii) $2 - x$, $1 - y$, z; (iii) $^1/_2 + y$, $-^1/_2 + x$, $2 - z$; (iv) $-x$, y, $^1/_2 - z$.

which is slightly less distorted at the higher temperature (based on Σ and Θ).[38,39] Since the distortion is influenced by crystal packing,[3] this temperature dependence should reflect changes to the lattice pressure about the molecule caused by anisotropic contraction of the crystal upon cooling. However, the magnitude of the distortion at both temperatures is sufficient that spin-crossover would not be expected in **2**, on the basis of previous work.[1]

Despite their distorted molecular structure, the complex cations in **2** pack into a version of the terpyridine embrace lattice[40] that is adopted by several salts of $[Fe(1\text{-}bpp)_2]^{2+}$ complexes with more regular six-coordinate geometries.[14,28−32] The cations associate into (approximately) 4-fold layers in the (001) crystal plane, by interdigitation of their pyrazolyl groups through face-to-face $\pi\cdots\pi$ contacts (Figure 3). The distances and angles between the least-squares planes of overlapping pyrazolyl groups are slightly different at the two temperatures, lying between 3.358(9) and 3.49(3) Å and between 5.9(6) and 8.07(13)°, respectively.
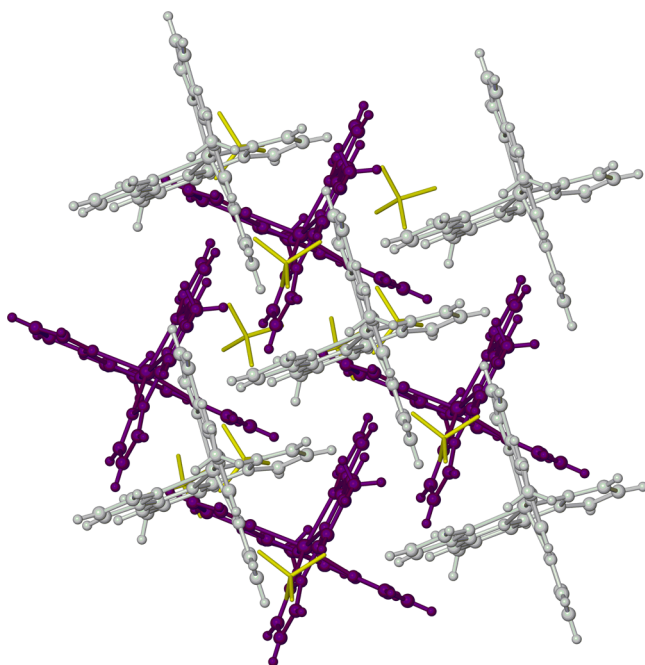
Figure 3. Packing diagram of **2**, showing the 4-fold interdigitation of the molecules into terpyridine embrace layers. Two of the four cation layers in the unit cell are shown, colored white and purple, and the yellow ClO_4^- anions are de-emphasized for clarity.

Figure 4. Comparison of room temperature X-ray powder diffraction data from **1** and **2**, with simulations based on the 240 K single crystal structure of **2**. The ClO_4^- ions were replaced by BF_4^- ions in the model for the simulation of **1**.

The high-spin PF_6^- salt **3** was also crystallographically characterized, and exhibits a more pronounced version of the Jahn−Teller distortion than **2**, with a reduction in θ to 67.70(2)° as well as in ϕ (157.92(9)°; Figure 2 and Table 1). Its high-spin nature is therefore more in line with precedent. Unlike **2**, **3** does not adopt a terpyridine embrace crystal lattice, and its complex molecules only interact through van der Waals contacts.

X-ray Powder Diffraction Data: A Low-Pressure Phase Transition. X-ray powder diffraction measurements showed that rapidly precipitated **1** and **2** are isostructural with each other, and with the solvent-free crystal phase of **2** (Figure 4). The diffraction peaks are significantly broader for **1**, however, implying that material is less crystalline than the perchlorate salt. Slowly cooling both samples below their spin-transition temperature at reduced pressure (10−20 Torr) led to their transformation to a new phase. The powder patterns of the low-temperature phases for the two compounds are similar, but significantly different from the room temperature materials (Figure 5). The phase transition temperatures in cooling mode were 193 ± 3 K for **1** and 160 ± 2 K for **2**. The slightly lower temperature of these phase transitions, compared to $T_{1/2}$ in the susceptibility data, could reflect the reduced pressures used in the powder diffraction measurement (see below) and/or small differences in the temperature calibration of the two instruments. In any case, a crystallographic phase change occurs in **1** and **2** between their high- and low-spin states, which is consistent with the decomposition of crystals of **2** upon slowly cooling them below $T_{1/2}$.

The variable temperature powder diffraction experiments were performed under vacuum, to prevent icing of the samples. Interestingly, the low-spin phase of both compounds was only observed below $T_{1/2}$ when the samples were measured at pressures above ca. 10 Torr. If the low-spin samples were evacuated to 10^{-5} Torr at 120 K, they spontaneously
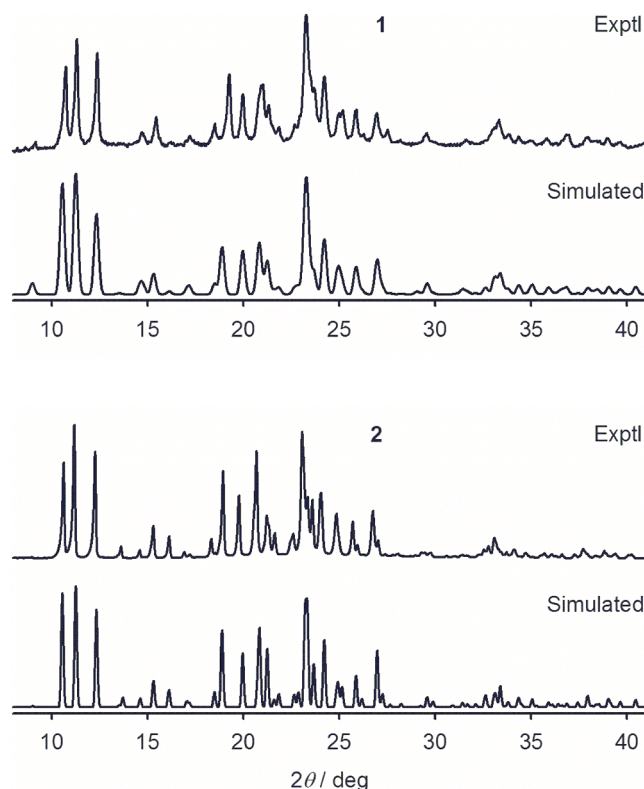
reconverted to the high-temperature crystal phase. The unit cell parameters from the low-pressure powder patterns, above and below their spin-crossover temperatures, are very similar (Table 3). In particular, the low-spin unit cell volume of a spin-crossover complex is typically 2−5% smaller than the high-spin volume, all other things being equal.[41] Since that is not observed in Table 3, the unit cell data imply that **1** and **2** may remain high-spin above 120 K at 10^{-5} Torr. However, application of the mean-field Clausius−Clapeyron equation to **1** (eq 1)[42]

$$\frac{\Delta T_{1/2}}{\Delta p} = \frac{\Delta V}{\Delta S} \tag{1}$$

with $\Delta T_{1/2} = -70$ K (reduction in $T_{1/2}$ to 120 K), $\Delta V = 20$ Å³ per molecule,[43] and $\Delta S = 50$ J mol^{-1} K^{-1} (from the DSC data) leads to $\Delta p = -3 \times 10^8$ Pa, substantially higher than employed in this experiment ($\Delta p = -10^5$ Pa). By the same criteria, 10^{-5} Torr vacuum (ca. 0 Pa) should lead to a reduction in $T_{1/2}$ of <0.1 K from its value under ambient conditions. Hence, the reduction in pressure in this experiment is insufficient to induce a low → high spin-transition at 10^{-5} Torr. Therefore, the most likely interpretation of these data is that the low-pressure phase transition in **1** and **2** is simply a crystallographic phase change, and that the materials remain low-spin below $T_{1/2}$ at 10^{-5} Torr. That being the case, the small volume change between the high-spin and low-spin materials at 10^{-5} Torr (Table 3) is unusual but not unprecedented.[44]

Photomagnetic Data and the LIESST Effect. Salts of $[Fe(bpp)_2]^{2+}$ derivatives are well-known to exhibit favorable photomagnetic effects at low temperatures.[14,29−31,34,35,45−47]
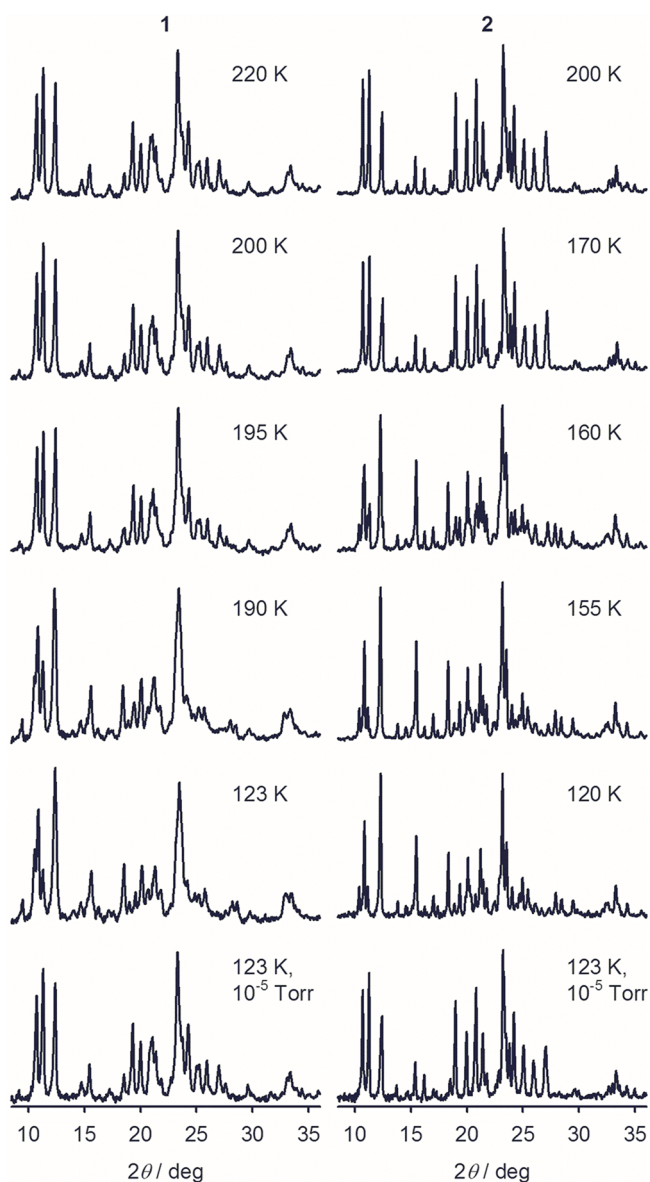
Figure 5. Variable temperature X-ray powder diffraction data from **1** (left) and **2** (right) on a cooling temperature ramp at 10–20 Torr pressure, and at 10^{-5} Torr at low temperature. The powder pattern of **2** at 160 K contains a mixture of the high- and low-temperature phases.

Table 3. Unit Cell Parameters from Rietveld Refinements of the High-Spin Phases of 1 and 2 under High Vacuum (10^{-5} Torr) above and below Their Thermal Spin-Transition Temperatures at Ambient Pressure

	1		**2**	
T (K)	240	170	220	150
a (Å)	8.521	8.512	8.530	8.515
b (Å)	8.587	8.581	8.628	8.614
c (Å)	39.717	39.664	40.354	40.316
β (deg)	101.37	101.39	101.68	101.87
V (Å^3)	2848.8	2840.0	2908.6	2893.8

The low-spin → high-spin photoconversion was therefore investigated in powder samples of **1** and **2**. The samples were irradiated at the following wavelengths: 405, 510, 640, 830, and 980 nm. In each case, the most efficient wavelength for inducing the LIESST effect was 510 nm, leading to a strong

increase of the magnetic signal at 10 K. No reverse-LIESST was observed upon irradiation with near-infrared wavelengths. Our previously reported T(LIESST) procedure[24−26,48] was followed to monitor the direct magnetic response on a thin layer of the compounds during and after irradiation in the $^1A_1 \rightarrow {}^1$MLCT absorption band (Figure 6).

For both complexes, a strong increase in the magnetic signal under green light irradiation was observed at 10 K. Following the irradiation procedure, an increase in $\chi_M T$ occurs upon heating from 10 K in the dark, reflecting zero-field splitting of the high-spin iron(II) centers.[49] The maximum values of $\chi_M T$ above ca. 30 K indicate a quantitative photoconversion efficiency (Figure 6). Above 70 K the metastable light-induced HS state decreases to reach the baseline. The T(LIESST) values can be extracted from the first derivative of the $\chi_M T$ vs T curves (Figure 6, inset) affording T(LIESST) = 87 and 112 K for **1** and **2**, respectively. In common with most other $[\text{Fe(bpp)}_2]^{2+}$ derivatives that have been measured by this procedure,[14,28−30] these values agree reasonably with predicted values according to the empirical eq 2 (T_0 = 150 K).[25,48]

$$T(\text{LIESST}) = T_0 - 0.3T_{1/2} \tag{2}$$

The T(LIESST) value for **2** is notably high, since spin-crossover compounds with T(LIESST) > 100 K are still unusual.[25,50−52]

The dynamics of LIESST relaxation of the photoinduced high-spin fraction of the sample (γ_{HS}) were investigated for both complexes in the temperature range 70−110 K, where high-spin → low-spin relaxation is thermally activated. The value of γ_{HS} was deduced from the equation $[(\chi_M T)_{h\nu} - (\chi_M T)_{LS}]/[(\chi_M T)_{HS} - (\chi_M T)_{LS}]$, where $(\chi_M T)_{h\nu}$ is the magnetic value reached after irradiation, $(\chi_M T)_{LS}$ is the magnetic value of the initial LS state at the given temperature, and $(\chi_M T)_{HS}$ is the magnetic value recorded at room temperature for a fully HS state. For both compounds, the relaxation behavior deviates strongly from a single exponential (Figure 7). The sigmoidal shape of the relaxation curves is consistent with the cooperative thermal spin-transitions. Therefore, the relaxation curves have been simulated according to Hauser's self-acceleration model, which reflects the change in the energy barrier as a function of γ_{HS} in cooperative SCO materials [eqs 3 and 4, where $\alpha = E_a^*/k_B T$ and $k_{HL} = k_\infty \exp(-E_a/k_B T)$]:[53]

$$\frac{\partial \gamma_{HS}}{\partial t} = -k_{HL}^* \gamma_{HS} \tag{3}$$

$$k_{HL}^*(T, \gamma_{HS}) = k_{HL}(T)\exp[a(T)(1 - \gamma_{HS})] \tag{4}$$

This procedure yielded the solid lines shown in Figure 7. Whereas the self-accelerated model reproduces the relaxation curves of **1** very well, it deviates slightly from the data for **2**. The discrepancy may imply a small distribution of activation energies for the relaxation process, since the experimental curves are smoother than the simulated ones. From these simulations, Arrhenius plots were drawn to extract the dynamical parameters (Figure 7, insets): E_a = 1300 cm^{-1}, E_a^* = 190 cm^{-1}, k_∞ = 0.98 × 10^6 s^{-1} for **1**, and E_a = 1645 cm^{-1}, E_a^* = 170 cm^{-1}, k_∞ = 1.02 × 10^6 s^{-1} for **2**. These values are comparable to those we have previously reported for other members of the $[\text{Fe(1-bpp)}_2]^{2+}$ series.[14,29,30,34,45] The lower value of E_a^* for **2** could reflect the aforementioned distribution of activation energies in its relaxation rate curves.

An elegant way to validate these simulation parameters is to reproduce the experimental T(LIESST) curves. The procedure
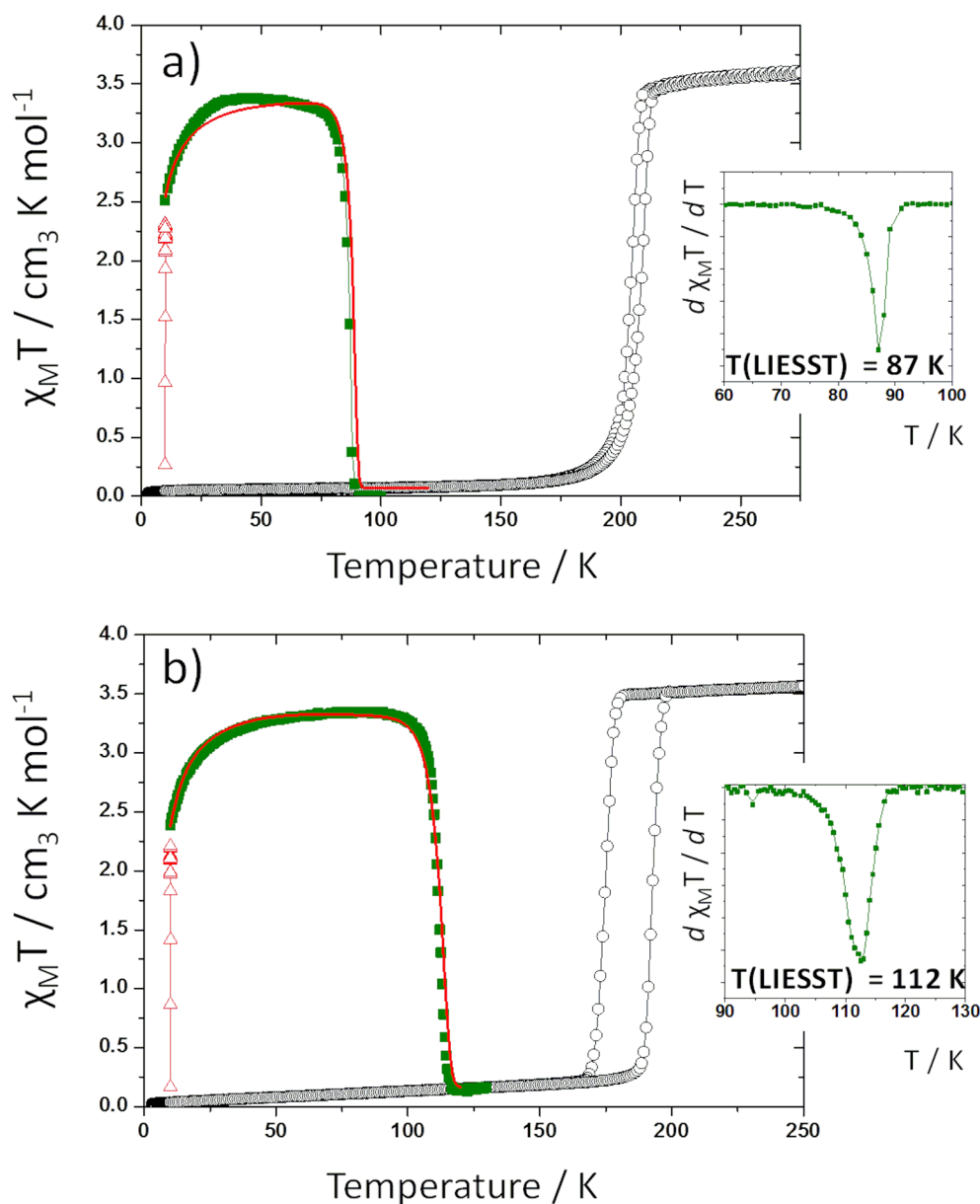
Figure 6. Temperature dependence of $\chi_M T$ for (a) **1** and (b) **2**: thermal behavior of $\chi_M T$ before irradiation (○), during irradiation (△) at 510 nm at 10 K, and the T(LIESST) measurement in the warming mode when the laser was switched off (◆). The red lines show the T(LIESST) simulations discussed in the text, with $g = 2.18$ and $D = 18$ cm^{-1}. Inset: first derivative of the $\chi_M T$ vs T curve, recorded in the dark after irradiation, whose minimum gives T(LIESST).

takes careful account of the time and temperature dependencies of the relaxation, and combines the quantum mechanical tunneling and the thermally activated regions (eq 5).[48,54]

$$\frac{\partial \gamma_{HS}}{\partial t} = -\gamma_{HS}\{k_0 + k_\infty \exp(-E_a/k_B T)\}\exp[\alpha(T)(1 - \gamma_{HS})]$$

(5)

The rate constant k_0 characterizes the relaxation in the quantum tunneling region, and is estimated as an upper limit from the last complete kinetic data obtained at the lowest temperature. A zero-field splitting contribution was also accounted for in the simulations, by introducing g and D values.[54] k_0 is of the order of 7×10^{-6} s^{-1} for **1** and 3×10^{-6} s^{-1} for **2**. The calculated T(LIESST) curves (Figure 6) show excellent agreement with the experimental T(LIESST) data, thereby validating the derived parameters and the simulation procedure.

The cooperative nature of the LIESST relaxation in these compounds was probed further by measuring light-induced thermal hysteresis (LITH) loops, which result from a competition between the permanent photoexcitation and the self-accelerated thermal relaxation process at temperatures near T(LIESST).[53,55] As expected, **1**, which has the less cooperative thermal spin-transition, exhibits a narrower LITH loop than that of **2** (Figure 8, green data). Interestingly, the cooling branch of the LITH hysteresis loop for **2** has an unusual two-step character, which is not apparent in the LIESST relaxation kinetics for **2** (despite the small distribution in relaxation rates), or on its thermal hysteresis loop at higher temperature. The LITH discontinuity might be associated with a reversal of the crystallographic phase change between the spin-states (Figure 5) as the low → high spin-photoconversion proceeds. That
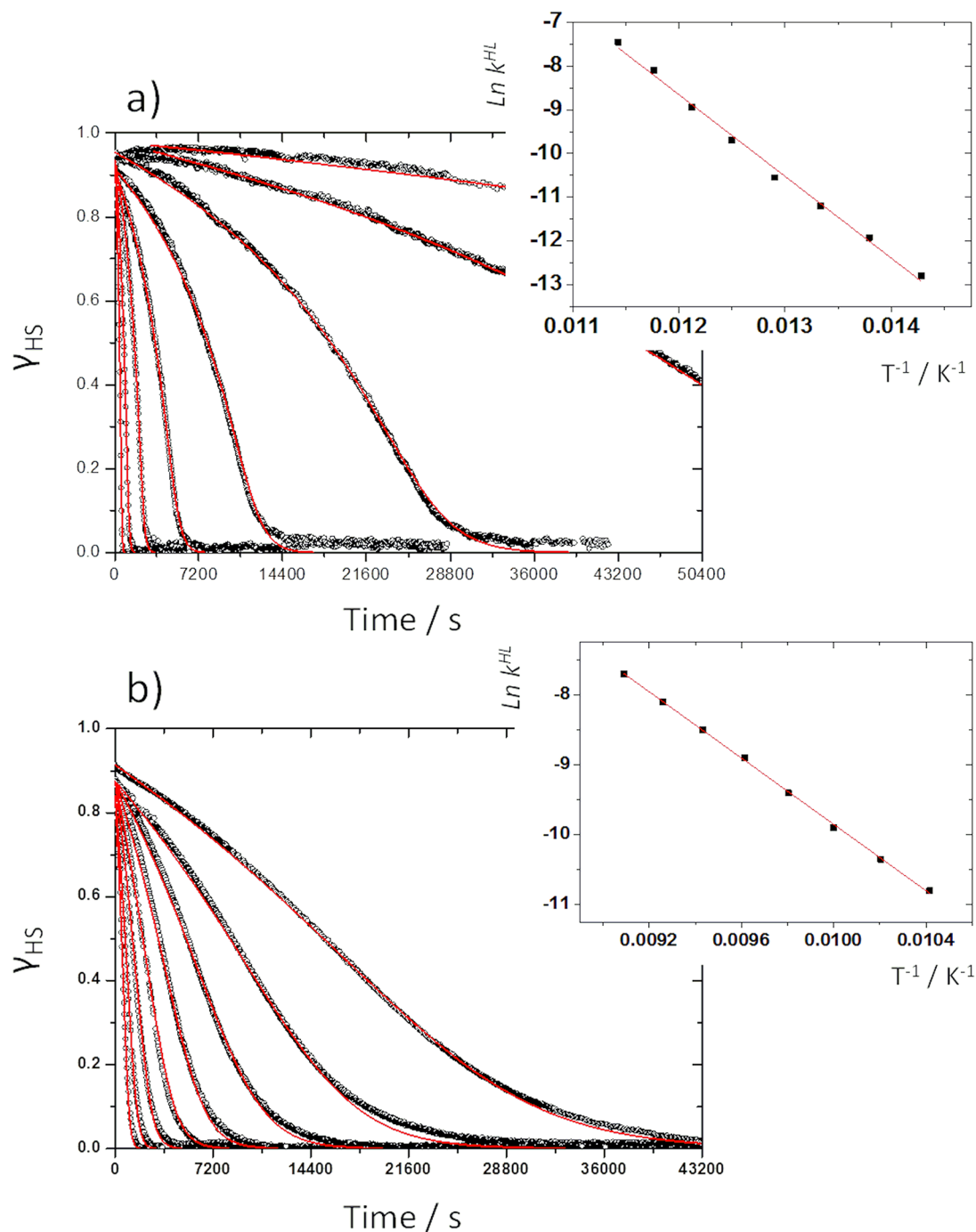
Figure 7. HS → LS relaxation for (a) **1** between 72 and 85 K and (b) **2** between 96 and 110 K. The relaxation curves are fitted according to Hauser's sigmoidal law.[53] Insets: Arrhenius plots of ln k_{HL} vs $1/T$, showing the line of best linear fit.

could be verified by photocrystallography, if single crystals of the low-spin state of **2** can be prepared.[41]

The shapes of these apparent LITH curves can be influenced by kinetic considerations, such as differing rates of light penetration through the dark low-spin and pale high-spin material. This can be clarified by measuring the evolution of the sample toward a photostationary state from a low-spin and the high-spin starting point, under constant irradiation at a particular temperature inside the hysteresis loop (Figure 8, red data). For **1**, the low-spin and high-spin states tend toward the same photostationary point over time at 86 K, indicating that its apparent LITH loop is purely a reflection of these

kinetic factors; there would be no LITH hysteresis for **1** if the sample were measured sufficiently slowly. In contrast, photostationary data were measured at three different temperatures for **2**. In each case, the photostationary spin-state populations from the high-spin and low-spin curves are different, showing that it retains a hysteretic spin-state conversion under constant irradiation even after the kinetic factors are accounted for. This is further evidence that spin-crossover by LIESST relaxation is more cooperative in **2** than in **1**.
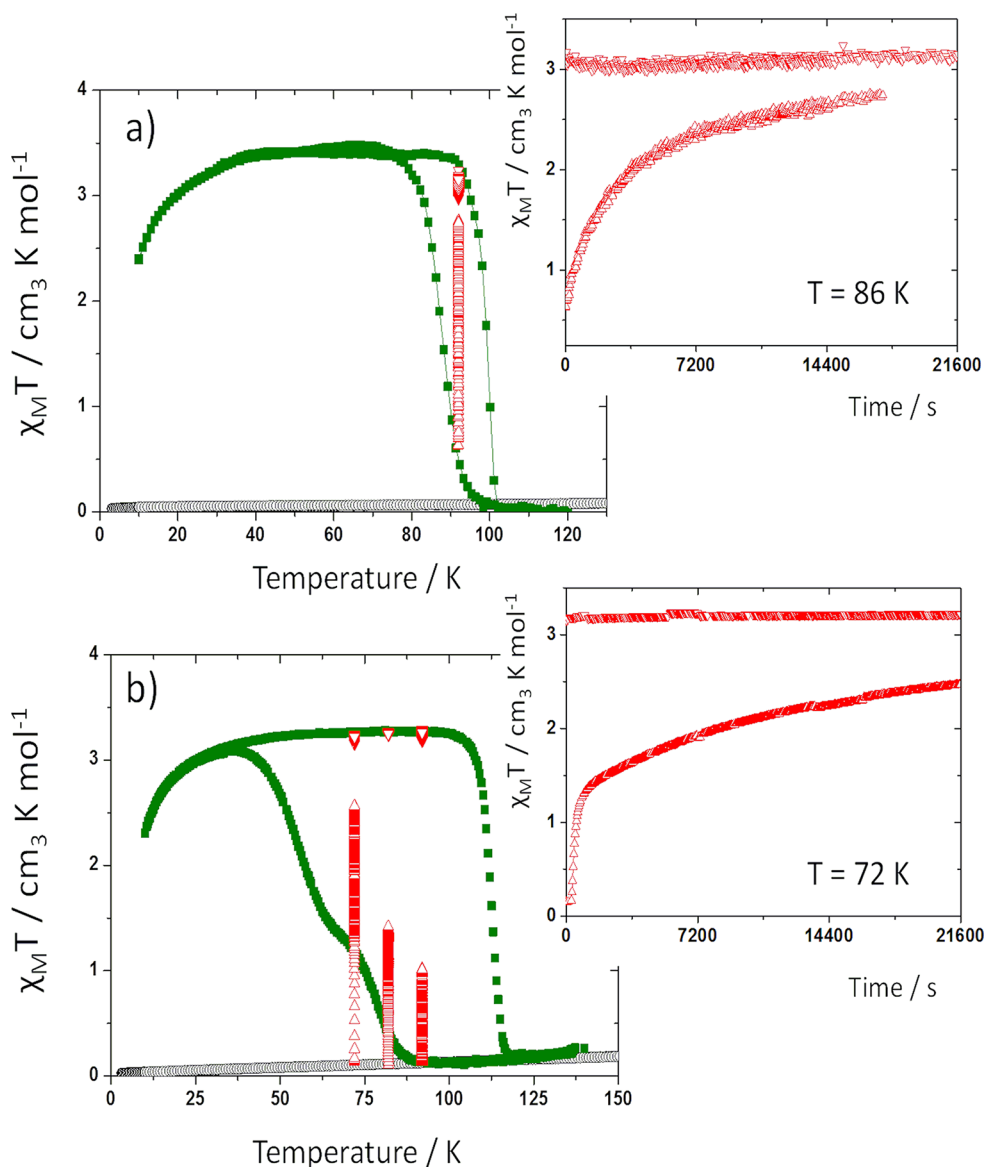
Figure 8. Temperature dependence under light irradiation at 510 nm of $\chi_M T$ for (a) **1** and (b) **2** giving rise to the LITH curves. Inset: Time dependence under light irradiation of $\chi_M T$ at a given temperature to record the photostationary states.

■ DISCUSSION

In an earlier survey, all $[Fe(1\text{-bpp})_2]^{2+}$ derivatives that were spin-crossover active exhibited comparable Jahn−Teller distortion parameters in their high-spin and low-spin forms, with $\phi \geq 172°$ and $\theta \geq 76°$ (Figure 9).[1] In fact, most of the high-spin complexes exhibit more distorted structures, with either or both of ϕ and θ lying outside this range. These examples are all high-spin between 5 and 300 K, which was proposed to reflect an unfavorable lattice activation energy, associated with their conversion to the less distorted coordination sphere adopted by their low-spin forms.[7] That is, solid $[Fe(1\text{-bpp})_2]^{2+}$ complexes are kinetically trapped in their high-spin state, if their structure deviates too strongly from the idealized D_{2d} symmetry preferred by low-spin $[Fe(1\text{-bpp})_2]^{2+}$ centers. That interpretation was recently confirmed by a computational study of different salts of $[Fe(1\text{-bpp})_2]^{2+}$, with distorted and undistorted geometries.[17]

However, **2** is one of three recently reported compounds from the $[Fe(1\text{-bpp})_2]^{2+}$ family that exhibit significantly greater Jahn−Teller distortions in their high-spin state, but are still

spin-crossover active (Figure 9). The other examples are **5**,[15] and molecule B in the structure of **6**[47,57] (Chart 2). Unlike **2**, structures of **5** and **6** are available in both spin states. Neither compound undergoes a crystallographic phase change during spin-crossover, and they both exhibit more regular molecular geometries in their low-spin forms as expected (Table 4). This transformation from a distorted high-spin to an undistorted low-spin form leads to an unusually large rearrangement of their molecular structure during the spin-transition, as evidenced by $\Delta\phi$ and $\Delta\theta$, the differences in those parameters between the high- and low-spin states (Table 4). In particular, **5** and **6** (molecule B) exhibit the largest values of $\Delta\phi$ yet reported for a spin-crossover complex from this family, while $\Delta\theta$ for **5** is also unusually large.[1,7]

All three compounds exhibit noteworthy cooperativity in their spin-transitions. Solid **2** and **5** both undergo hysteretic spin-transitions near 160−170 K, with $\Delta T_{1/2} = 15−18$ K. The thermal hysteresis in **2**, which adopts a terpyridine embrace crystal lattice (Figure 3), is wider than usual for $[Fe(1\text{-bpp})_2]^{2+}$ derivatives with this structure type ($\Delta T_{1/2} \leq 4$ K is more
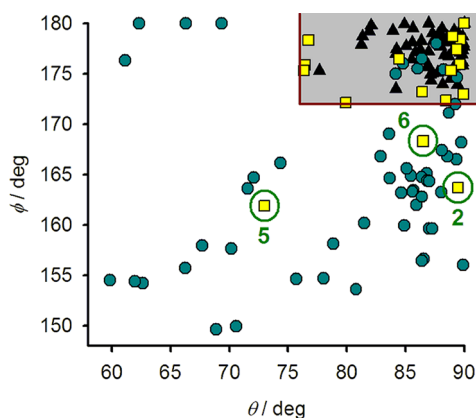
Figure 9. Jahn–Teller distortion parameters (Chart 1) from crystal structures of $[Fe(1-bpp)_2]^{2+}$ derivatives that are low-spin (black ▲); high-spin and spin-crossover active (yellow ■); and high-spin and spin-crossover inactive (cyan ●). The distortion range that is normally consistent with spin-crossover activity is shaded, and the three anomalous spin-crossover compounds lying outside this range are highlighted (Chart 2).[56]

Chart 2. Literature Compounds Highlighted in Figure 9 and Table 3
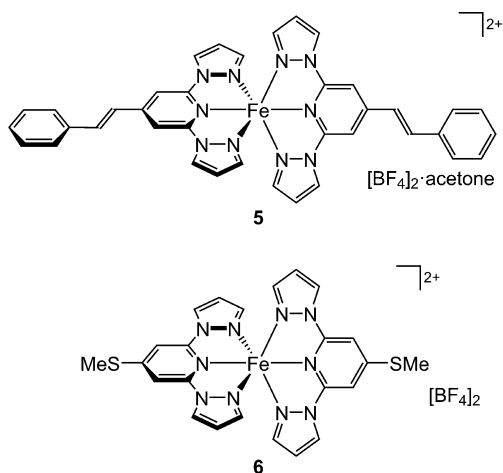
Table 4. Spin-Transition Temperatures for the Three Highlighted Complexes in Figure 9 (Chart 2) and Their Jahn–Teller Distortion Parameters in Their High-Spin and Low-Spin Crystal Structures[a]

	2	**5**[15]	**6, molecule B**[47,57]
$T_{1/2}\downarrow$	175	164	268
$T_{1/2}\uparrow$	193	179	270
$\Delta T_{1/2}$	18	15	2
ϕ (high-spin)	163.7(2)	161.92(10)	168.3(2)
ϕ (low-spin)		175.25(13)	175.2(2)
$\Delta\phi$		13.33(16)	6.9(3)
θ (high-spin)	89.48(7)	73.00	86.55(5)
θ (low-spin)		77.65	87.76(4)
$\Delta\theta$		4.65	1.21(6)

[a]$\Delta\phi$ and $\Delta\theta$ are the differences in those parameters between the high- and low-spin structures. Data from other compounds from the $[Fe(1-bpp)_2]^{2+}$ family are listed in the Supporting Information.

typical[14,32]). A similar comparison is more difficult for **5** since there are no data from related compounds, but there are no

strong π–π interactions or other intermolecular contacts in the lattice of **5** that could account for its spin-crossover cooperativity, *per se*.[7] Spin-crossover in molecule B of **6** is less remarkable, with only a narrow thermal hysteresis ($\Delta T_{1/2}$ = 2 K). However, this is still more cooperative than molecule A in the same material,[57] as well as two other complex salts that are almost isostructural to **6**, show more regular values of θ and ϕ, and exhibit gradual thermal spin-crossover equilibria.[47]

Cooperative spin-crossover switching in molecular materials is a function of the magnitude of the structure change between the spin-states, and intermolecular interactions between the switching centers to propagate that structure change through the bulk material.[7] Solid **2**, **5**, and **6** all exhibit more cooperative spin-transitions than expected on the basis of their crystal packing, taken in isolation. Therefore, this can be attributed to the large molecular structure rearrangement during spin-crossover that is associated with their unusually distorted high-spin forms.

The relationship between molecular structure and the temperature of spin-crossover is also of interest. An earlier survey of $[Fe(NCS)_2L_2]$ (L = a bidentate heterocyclic N-donor ligand) complexes demonstrated a linear relationship between the distortion of the metal ion coordination sphere and the spin-crossover temperature.[58] Larger trigonal distortions of the metal ion coordination sphere away from O_h symmetry tend to stabilize the high-spin state in those compounds, thus reducing $T_{1/2}$ and increasing T(LIESST). Although those conclusions are comparable to the discussion in this work, there is no simple relationship between $T_{1/2}$, and the distortion parameters in Tables 2 and 4, for $[Fe(1-bpp)_2]^{2+}$ derivatives (plotted in the Supporting Information).[7] In practice, such a relationship would have to take account of the inductive properties of any bpp ligand substituents, which can have a significant effect on the ligand field of $[Fe(1-bpp)_2]^{2+}$ derivatives.[1] An investigation toward that end is in progress, and will be reported separately.

■ **CONCLUSIONS**

This study, and consideration of other recent work,[15,47] necessitates a modification of our previous proposal that spin-crossover in salts of $[Fe(1-bpp)_2]^{2+}$ derivatives is inhibited for Jahn–Teller distorted high-spin compounds with $\phi < 172°$ and/or $\theta < 76°$ (Chart 1). While that rule still holds in the majority of cases (Figure 9), three examples are now known that are spin-crossover active despite having larger distortions in their high-spin states. Evidently the solid lattices in these specific materials are unusually deformable, to permit the large structural rearrangements associated with their spin-crossover.

These exceptional compounds also exhibit more cooperative spin-transitions that might be expected from consideration of their crystal packing. Thus, **2** exhibits a significantly wider thermal hysteresis than any other $[Fe(1-bpp)_2]^{2+}$ derivative with a terpyridine embrace type lattice.[14,28−32] In **5** and **6**, the change in molecular structure associated with quenching of the Jahn–Teller distortion in the low-spin state is unusually large compared to those of other compounds from the $[Fe(1-bpp)_2]^{2+}$ family (Table 4 and the Supporting Information). The same is likely to be true in **2**, although its low-spin crystal structure could not be determined. Hence, Jahn–Teller distortions in high-spin $[Fe(1-bpp)_2]^{2+}$ derivatives promote cooperativity in spin-crossover, when they are not too large to prevent it from occurring. That is consistent with our wider considerations of structure:function relationships in spin-transition materials, where abrupt and hysteretic transitions

are promoted by a large change in molecular structure between the spin states.[7]

Compounds **1** and **2** also exhibit a reversible transformation at low temperatures back to their room temperature crystal phase, under 10^{-5} Torr pressure inside a powder diffractometer. Since the tendency of high-pressure to stabilize the low-spin states of iron complexes is well-known,[41,42] it is tempting to conclude that a vacuum-induced low → high spin-state change is occurring in **1** and **2**. However, thermodynamic considerations imply that such a transition would require a pressure change ca. 1000 times larger than that in our experiment (eq 1). Hence the low-pressure phases of the materials almost certainly contain low-spin complex molecules, despite their similarity to the high-spin materials by the powder diffraction technique.

■ ASSOCIATED CONTENT

Ⓢ Supporting Information

Definitions of the structural indices used in Table 1, additional crystallographic figures and tables, magnetic susceptibility data, and crystallographic information files (CIFs). The Supporting Information is available free of charge on the ACS Publications website at DOI: 10.1021/acs.inorgchem.5b00614. CCDC 1006380 (**1**·4MeNO$_2$), 1006381 (**2**·4MeNO$_2$), 1006382 (**2** at 240 K), 1006383 (**2** at 100 K), and 1006384 (**3**) containing the supplementary crystallographic data can be obtained free of charge from the Cambridge Crystallographic Data Center via www.ccdc.cam.ac.uk/data_request/cif.

■ AUTHOR INFORMATION

Corresponding Authors
*E-mail: chastanet@icmcb-bordeaux.cnrs.fr.
*E-mail: m.a.halcrow@leeds.ac.uk.
Notes
The authors declare no competing financial interest.

■ ACKNOWLEDGMENTS

■ REFERENCES

(1) Halcrow, M. A. *Coord. Chem. Rev.* **2009**, *253*, 2493−2514.
(2) Olguín, J.; Brooker, S. *Coord. Chem. Rev.* **2011**, *255*, 203−240.
(3) Kershaw Cook, L. J.; Mohammed, R.; Sherborne, G.; Roberts, T. D.; Alvarez, S.; Halcrow, M. A. *Coord. Chem. Rev.* **2015**, *289−290*, 2−12.
(4) *Spin Crossover in Transition Metal Compounds I−III, Topics in Current Chemistry*; Gütlich, P., Goodwin, H. A., Eds.; Springer-Verlag: Berlin, 2004; Vols. *233−235*.
(5) *Spin-Crossover Materials—Properties and Applications*; Halcrow, M. A., Ed.; John Wiley & Sons, Ltd.: New York, 2013; p 568.
(6) (a) Bousseksou, A.; Molnár, G.; Salmon, L.; Nicolazzi, W. *Chem. Soc. Rev.* **2011**, *40*, 3313−3335. (b) Cavallini, M. *Phys. Chem. Chem. Phys.* **2012**, *14*, 11867−11876. (c) Shepherd, H. J.; Molnár, G.; Nicolazzi, W.; Salmon, L.; Bousseksou, A. *Eur. J. Inorg. Chem.* **2013**, 653−661.
(7) Halcrow, M. A. *Chem. Soc. Rev.* **2011**, *40*, 4119−4142.
(8) For other recent reviews see: (a) Muñoz, M. C.; Real, J. A. *Coord. Chem. Rev.* **2011**, *255*, 2068−2093. (b) Tao, J.; Wei, R.-J.; Huang, R.-B.; Zheng, L.-S. *Chem. Soc. Rev.* **2012**, *41*, 703−737. (c) Gütlich, P.

(d) Gütlich, P.; Gaspar, A. B.; Garcia, Y. *Beilstein J. Org. Chem.* **2013**, *9*, 342−391.
(9) Holland, J. M.; McAllister, J. A.; Kilner, C. A.; Thornton-Pett, M.; Bridgeman, A. J.; Halcrow, M. A. *J. Chem. Soc., Dalton Trans.* **2002**, 548−554.
(10) Elhaïk, J.; Evans, D. J.; Kilner, C. A.; Halcrow, M. A. *Dalton Trans.* **2005**, 1693−1700.
(11) Elhaïk, J.; Kilner, C. A.; Halcrow, M. A. *Dalton Trans.* **2006**, 823−830.
(12) (a) Elhaïk, J.; Kilner, C. A.; Halcrow, M. A. *CrystEngComm* **2005**, *7*, 151−157. (b) Kilner, C. A.; Halcrow, M. A. *Polyhedron* **2006**, *25*, 235−240.
(13) Haryono, M.; Heinemann, F. W.; Petukhov, K.; Gieb, K.; Müller, P.; Grohmann, A. *Eur. J. Inorg. Chem.* **2009**, 2136−2143.
(14) Mohammed, R.; Chastanet, G.; Tuna, F.; Malkin, T. L.; Barrett, S. A.; Kilner, C. A.; Létard, J.-F.; Halcrow, M. A. *Eur. J. Inorg. Chem.* **2013**, 819−831.
(15) Hasegawa, Y.; Sakamoto, R.; Takahashi, K.; Nishihara, H. *Inorg. Chem.* **2013**, *52*, 1658−1665.
(16) Although they are not discussed in those terms, the following references also contain Jahn−Teller distorted [Fe(bpp)$_2$]$^{2+}$ derivatives: (a) Nihei, M.; Han, L.; Tahira, H.; Oshio, H. *Inorg. Chim. Acta* **2008**, *361*, 3926−3930. (b) González-Prieto, R.; Fleury, B.; Schramm, F.; Zoppellaro, G.; Chandrasekar, R.; Fuhr, O.; Lebedkin, S.; Kappes, M.; Ruben, M. *Dalton Trans.* **2011**, *40*, 7564−7570.
(17) Vela, S.; Novoa, J. J.; Ribas-Arino, J. *Phys. Chem. Chem. Phys.* **2014**, *16*, 27012−27024.
(18) Examples of the angular Jahn−Teller distortion in derivatives of [Fe(3-bpp)$_2$]$^{2+}$ (3-bpp = 2,6-di(pyrazol-3-yl)pyridine, an isomer of 1-bpp): (a) Craig, G. A.; Roubeau, O.; Aromí, G. *Coord. Chem. Rev.* **2014**, *269*, 13−31 and references therein. (b) Roberts, T. D.; Little, M. A.; Kershaw Cook, L. J.; Barrett, S. A.; Tuna, F.; Halcrow, M. A. *Polyhedron* **2013**, *64*, 4−12. (c) Roberts, T. D.; Little, M. A.; Kershaw Cook, L. J.; Halcrow, M. A. *Dalton Trans.* **2014**, *43*, 7577−7588. (d) Barrios, L. A.; Peyrecave-Lleixà, E.; Craig, G. A.; Roubeau, O.; Teat, S. J.; Aromí, G. *Eur. J. Inorg. Chem.* **2014**, 6013−6021.
(19) Examples of the angular Jahn−Teller distortion in high-spin derivatives of [Fe(terpy)$_2$]$^{2+}$ (terpy = 2,2′:6′,2″-terpyridine): (a) Constable, E. C.; Baum, G.; Bill, E.; Dyson, R.; van Eldik, R.; Fenske, D.; Kaderli, S.; Morris, D.; Neubrand, A.; Neuburger, M.; Smith, D. R.; Wieghardt, K.; Zehnder, M.; Zuberbühler, A. D. *Chem.—Eur. J.* **1999**, *5*, 498−508. (b) Pelascini, F.; Wesolek, M.; Peruch, F.; De Cian, A.; Kyritsakas, N.; Lutz, P. J.; Kress, J. *Polyhedron* **2004**, *23*, 3193−3199. (c) Brauchli, S. Y.; Constable, E. C.; Harris, K.; Häussinger, D.; Housecroft, C. E.; Rösel, P. J.; Zampese, J. A. *Dalton Trans.* **2010**, *39*, 10739−10748.
(20) Other examples of the angular distortion in six-coordinate d^5 or d^6 metal complexes: (a) Rajan, R.; Rajaram, R.; Nair, B. U.; Ramasami, T.; Mandal, S. K. *J. Chem. Soc., Dalton Trans.* **1996**, 2019−2021. (b) Glynn, C. W.; Turnbull, M. M. *Transition Met. Chem.* **2002**, *27*, 822−831. (c) Stupka, G.; Gremaud, L.; Bernardinelli, G.; Williams, A. F. *Dalton Trans.* **2004**, 407−412. (d) Hammes, B. S.; Damiano, B. J.; Tobash, P. H.; Hidalgo, M. J.; Yap, G. P. A. *Inorg. Chem. Commun.* **2005**, *8*, 513−516. (e) Baia, X.-Q.; Zhang, S.-H. *Acta Crystallogr., Sect. E* **2009**, *65*, m397. (f) Shang, S.-M.; Ren, C.-X.; Wang, X.; Lu, L.-D.; Yang, X.-J. *Acta Crystallogr., Sect. E* **2009**, *65*, m1023−m1024. (g) Wu, H.; Huang, X.; Yuan, J.; Kou, F.; Jia, F.; Liu, B.; Wang, K. *Eur. J. Med. Chem.* **2010**, *45*, 5324−5330.
(21) Sheldrick, G. M. *Acta Crystallogr., Sect. A* **2008**, *64*, 112−122.
(22) Barbour, L. J. *J. Supramol. Chem.* **2001**, *1*, 189−191.
(23) O'Connor, C. J. *Prog. Inorg. Chem.* **1982**, *29*, 203−283.
(24) Létard, J.-F.; Guionneau, P.; Rabardel, L.; Howard, J. A. K.; Goeta, A.; Chasseau, D.; Kahn, O. *Inorg. Chem.* **1998**, *37*, 4432−4441.
(25) Marcen, S.; Lecren, L.; Capes, L.; Goodwin, H. A.; Létard, J.-F. *Chem. Phys. Lett.* **2002**, *358*, 87−95.
(26) (a) Létard, J.-F.; Guionneau, P.; Nguyen, O.; Costa, J. S.; Marcen, S.; Chastanet, G.; Marchivie, M.; Capes, L. *Chem.—Eur. J.* **2005**, *11*, 4582−4589. (b) Létard, J.-F.; Chastanet, G.; Guionneau, P.; Desplanches, C. In *Spin-Crossover Materials—Properties and Applica-*

tions; Halcrow, M. A., Ed.; John Wiley & Sons: Chichester, U.K., 2013; Chapter 19, pp 475–506.

(27) Jameson, D. L.; Goldsby, K. A. *J. Org. Chem.* **1990**, *55*, 4992–4994.

(28) (a) Elhaïk, J.; Money, V. A.; Barrett, S. A.; Kilner, C. A.; Evans, I. R.; Halcrow, M. A. *Dalton Trans.* **2003**, 2053–2060. (b) Money, V. A.; Evans, I. R.; Elhaïk, J.; Halcrow, M. A.; Howard, J. A. K. *Acta Crystallogr., Sect. B* **2004**, *60*, 41–45.

(29) Carbonera, C.; Costa, J. S.; Money, V. A.; Elhaïk, J.; Howard, J. A. K.; Halcrow, M. A.; Létard, J.-F. *Dalton Trans.* **2006**, 3058–3066.

(30) Pritchard, R.; Lazar, H.; Barrett, S. A.; Kilner, C. A.; Asthana, S.; Carbonera, C.; Létard, J.-F.; Halcrow, M. A. *Dalton Trans.* **2009**, 6656–6666.

(31) Abhervé, A.; Clemente-León, M.; Coronado, E.; Gómez-García, C. J.; López-Jordà, M. *Dalton Trans.* **2014**, *43*, 9406–9409.

(32) (a) Pritchard, R.; Kilner, C. A.; Halcrow, M. A. *Chem. Commun.* **2007**, 577–579. (b) Santoro, A.; Kershaw Cook, L. J.; Kulmaczewski, R.; Barrett, S. A.; Cespedes, O.; Halcrow, M. A. *Inorg. Chem.* **2015**, *54*, 682–693.

(33) (a) Šalitroš, I.; Pavlik, J.; Boča, R.; Fuhr, O.; Rajadurai, C.; Ruben, M. *CrystEngComm* **2010**, *12*, 2361–2368. (b) Šalitroš, I.; Fuhr, O.; Eichhöfer, A.; Kruk, R.; Pavlik, J.; Dlháň, L.; Boča, R.; Ruben, M. *Dalton Trans.* **2012**, *41*, 5163–5171.

(34) Money, V. A.; Carbonera, C.; Elhaïk, J.; Halcrow, M. A.; Howard, J. A. K.; Létard, J.-F. *Chem.—Eur. J.* **2007**, *13*, 5503–5514.

(35) Nihei, M.; Tahira, H.; Takahashi, N.; Otake, Y.; Yamamura, Y.; Saito, K.; Oshio, H. *J. Am. Chem. Soc.* **2010**, *132*, 3553–3560.

(36) Sorai, M.; Nakazawa, Y.; Nakano, M.; Miyazaki, Y. *Chem. Rev.* **2013**, *113*, PR41–PR122.

(37) See, e.g.: (a) Ritter, G.; König, E.; Irler, W.; Goodwin, H. A. *Inorg. Chem.* **1978**, *17*, 224–228. (b) Buchen, T.; Gütlich, P.; Sugiyarto, K. H.; Goodwin, H. A. *Chem.—Eur. J.* **1996**, *2*, 1134–1138. (c) Hinek, R.; Spiering, H.; Gutlich, P.; Hauser, A. *Chem.—Eur. J.* **1996**, *2*, 1435–1439. (d) Roubeau, O.; Stassen, A. F.; Gramage, I. F.; Codjovi, E.; Linarès, J.; Varret, F.; Haasnoot, J. G.; Reedijk, J. *Polyhedron* **2001**, *20*, 1709–1716. (e) Marchivie, M.; Guionneau, P.; Létard, J.-F.; Chasseau, D.; Howard, J. A. K. *J. Phys. Chem. Solids* **2004**, *65*, 17–23. (f) Létard, J.-F.; Asthana, S.; Shepherd, H. J.; Guionneau, P.; Goeta, A. E.; Suemura, N.; Ishikawa, R.; Kaizaki, S. *Chem.—Eur. J.* **2012**, *18*, 5924–5934. (g) Craig, G. A.; Costa, J. S.; Teat, S. J.; Roubeau, O.; Yufit, D. S.; Howard, J. A. K.; Aromí, G. *Inorg. Chem.* **2013**, *52*, 7203–7209. (h) Murnaghan, K. D.; Carbonera, C.; Toupet, L.; Griffin, M.; Dirtu, M. M.; Desplanches, C.; Garcia, Y.; Collet, E.; Létard, J.-F.; Morgan, G. G. *Chem.—Eur. J.* **2014**, *20*, 5613–5618.

(38) α is the average of the four internal *cis*-N–Fe–N angles within the two chelate ligands, which increases from *ca.* 73° in the high-spin state to 80° in the low-spin state. Σ is a general measure of the deviation of a metal ion from an ideal octahedral geometry, while Θ more specifically indicates its distortion towards a trigonal prismatic structure.[39] Both Σ and Θ are usually much larger in the high-spin than in the low-spin state; a perfectly octahedral complex gives $\Sigma = \Theta = 0$. Mathematical definitions of Σ and Θ are in ref 39, and in the Supporting Information to this Article.

(39) (a) McCusker, J. K.; Rheingold, A. L.; Hendrickson, D. N. *Inorg. Chem.* **1996**, *35*, 2100–2112. (b) Guionneau, P.; Marchivie, M.; Bravic, G.; Létard, J.-F.; Chasseau, D. *Top. Curr. Chem.* **2004**, *234*, 97–128.

(40) Dance, I.; Scudder, M. *CrystEngComm* **2009**, *11*, 2233–2247.

(41) Guionneau, P. *Dalton Trans.* **2014**, *43*, 382–393.

(42) Gütlich, P.; Ksenofontov, V.; Gaspar, A. B. *Coord. Chem. Rev.* **2005**, *249*, 1811–1829.

(43) Holland, J. M.; McAllister, J. A.; Lu, Z.; Kilner, C. A.; Thornton-Pett, M.; Halcrow, M. A. *Chem. Commun.* **2001**, 577–578.

(44) Shepherd, H. J.; Palamarciuc, T.; Rosa, P.; Guionneau, P.; Molnár, G.; Létard, J.-F.; Bousseksou, A. *Angew. Chem., Int. Ed.* **2012**, *51*, 3910–3914.

(45) Chastanet, G.; Tovee, C. A.; Hyett, G.; Halcrow, M. A.; Létard, J.-F. *Dalton Trans.* **2012**, *41*, 4896–4902.

(46) Šalitroš, I.; Pogány, L.; Ruben, M.; Boča, R.; Linert, W. *Dalton Trans.* **2014**, *43*, 16584–16587.

(47) Kershaw Cook, L. J.; Shepherd, H. J.; Comyn, T. P.; Baldé, C.; Cespedes, O.; Chastanet, G.; Halcrow, M. A. *Chem.—Eur. J.* **2015**, *21*, 4805–4816.

(48) Létard, J.-F. *J. Mater. Chem.* **2006**, *16*, 2550–2559.

(49) Kahn, O. *Molecular Magnetism*; VCH: Weinheim, Germany, 1993.

(50) (a) Hayami, S.; Gu, Z.-Z.; Einaga, Y.; Kobayasi, Y.; Ishikawa, Y.; Yamada, Y.; Fujishima, A.; Sato, O. *Inorg. Chem.* **2001**, *40*, 3240–3242. (b) Costa, J. S.; Baldé, C.; Carbonera, C.; Denux, D.; Wattiaux, A.; Desplanches, C.; Ader, J.-P.; Gütlich, P.; Létard, J.-F. *Inorg. Chem.* **2007**, *46*, 4114–4119. (c) Wang, H.; Desplanches, C.; Dagault, P.; Létard, J.-F. *Dalton Trans.* **2014**, *43*, 15346–15350.

(51) (a) Hayami, S.; Gu, Z.-Z.; Shiro, M.; Einaga, Y.; Fujishima, A.; Sato, O. *J. Am. Chem. Soc.* **2000**, *122*, 7126–7127. (b) Hayami, S.; Hiki, K.; Kawahara, T.; Maeda, Y.; Urakami, D.; Inoue, K.; Ohama, M.; Kawata, S.; Sato, O. *Chem.—Eur. J.* **2009**, *15*, 3497–3508. (c) Craig, G. A.; Costa, J. S.; Roubeau, O.; Teat, S. J.; Shepherd, H. J.; Lopes, M.; Molnár, G.; Bousseksou, A.; Aromí, G. *Dalton Trans.* **2014**, *43*, 729–737.

(52) Higher thermal relaxation temperatures have sometimes been observed for charge-transfer spin-state trapping in Prussian blue analogue materials: (a) Shimamoto, N.; Ohkoshi, S.-I.; Sato, O.; Hashimoto, K. *Inorg. Chem.* **2002**, *41*, 678–684. (b) Li, D.; Clérac, R.; Roubeau, O.; Harté, E.; Mathonière, C.; Le Bris, R.; Holmes, S. M. *J. Am. Chem. Soc.* **2008**, *130*, 252–258.

(53) (a) Hauser, A. *Coord. Chem. Rev.* **1991**, *111*, 275–290. (b) Hauser, A.; Jeftić, J.; Romstedt, H.; Hinek, R.; Spiering, H. *Coord. Chem. Rev.* **1999**, *190–192*, 471–491. (c) Hauser, A.; Enachescu, C.; Daku, M. L.; Vargas, A.; Amstutz, N. *Coord. Chem. Rev.* **2006**, *250*, 1642–1652.

(54) Létard, J.-F.; Chastanet, G.; Nguyen, O.; Marcèn, S.; Marchivie, M.; Guionneau, P.; Chasseau, D.; Gütlich, P. *Monatsh. Chem.* **2003**, *134*, 165–182.

(55) (a) Desaix, A.; Roubeau, O.; Jeftić, J.; Haasnoot, J. G.; Boukheddaden, K.; Codjovi, E.; Linarès, J.; Nogues, M.; Varret, F. *Eur. Phys. J. B* **1998**, *6*, 183–193. (b) Enachescu, C.; Tanasa, R.; Stancu, A.; Chastanet, G.; Létard, J.-F.; Linarès, J.; Varret, F. *J. Appl. Phys.* **2006**, *99*, 08J504/1–08J504/3.

(56) Compounds in the shaded, spin-crossover region of Figure 6 that remain high-spin on cooling have bulky substituents or a twisted ligand conformation that sterically inhibit contraction of the metal coordination sphere. See refs 10 and 11, and the following: (a) Holland, J. M.; Barrett, S. A.; Kilner, C. A.; Halcrow, M. A. *Inorg. Chem. Commun.* **2002**, *5*, 328–332. (b) Han, L.; Nihei, M.; Oshio, H. *Polyhedron* **2005**, *24*, 2409–2412.

(57) The asymmetric unit of **6** around its spin-transition temperature contains two unique molecules. The other molecule (molecule A) exhibits more typical values of ϕ [178.6(3)°] and θ [89.04(5)°] in its high-spin state, and undergoes spin-crossover as a more gradual thermal equilibrium. See ref 47 for more details.

(58) Marchivie, M.; Guionneau, P.; Létard, J.-F.; Chasseau, D. *Acta Crystallogr., Sect. B* **2005**, *61*, 25–28. The distortion index considered in this study, θ_{NCS}, is related to the Θ parameter used in this work (Supporting Information).